Journal of the Korean Electrochemical Society
Vol. 27, No. 1, 2024, 15-31
https://doi.org/10.5229/JKES.2024.27.1.15

Research Paper
pISSN 1229-1935
eISSN 2288-9000

Electrochemical Detection of Hydroxychloroquine Sulphate Drug using CuO/GO Nanocomposite Modified Carbon Paste Electrode and its Photocatalytic Degradation

G. S. Shaila, Dinesh Patil, Naeemakhtar Momin, and J. Manjanna*
Dept. of Chemistry, Rani Channamma University, Belagavi 591156, Karnataka, India

(Received July 6, 2023 : Revised December 1, 2023 : Accepted December 13, 2023)

ABSTRACT

The antimalarial drug hydroxychloroquine sulphate (HCQ) has taken much attention during the first COVID-19 pandemic phase for the treatment of severe acute respiratory infection (SARI) patients. Hence it is interest to study the electrochemical properties and photocatalytic degradation of the HCQ drug. Copper oxide (CuO) nanoparticles, graphene oxide (GO) and CuO/GO NC (nanocomposite) modified carbon paste electrodes (MCPE) are used for the detection of HCQ in an aqueous medium. Electrochemical behaviour of HCQ (20 μM) was observed using CuO/MCPE, GO/MCPE and CuO/GO NC/MCPE in 0.1 M phosphate buffer at pH 7 with a scan rate of 20 to 120 mV s^{-1} by cyclic voltammetry (CV). Differential pulse voltammetry (DPV) of HCQ was performed for 0.6 to 16 μM HCQ. The CuO/GO NC/MCPE showed a reasonably good sensitivity of 0.33 to 0.44 μA μM cm^{-2} with LOD of 69 to 92 nM for HCQ. Furthermore, the CuO/GO NC was used as a catalyst for the photodegradation of HCQ by monitoring its UV-Vis absorption spectra. About 98% was degraded in about 34 min under visible light and after 4 cycles it was 87%. The improved photocatalytic activity may be attributed to decrease in bandgap energy and enhanced ability for the electrons to migrate. Thus, CuO/GO NC showed good results for both sensing and degradation applications as well as reproducibility.

Keywords : Hydroxychloroquine sulphate (HCQ), CuO/GO nanocomposite, Voltammetry, Photocatalytic degradation

1. Introduction

The coronavirus causes SARS-COV-2 (severe acute respiratory syndrome) and spreads through close contact with the affected person by inhaling the droplet during sneezing and coughing. The first case was discovered in Wuhan (China) in December 2019 and gradually spread all over the world. Considering the seriousness of the coronavirus outbreak, WHO declared this viral disease as a pandemic on 11th March 2020.[1] Since then, across national borders, the virus has spread, affecting millions of people around the world. The chloroquine (CQ) and hydroxychloroquine sulphate (HCQS/HCQ) have been tagged as probable 'Game-changers' for COVID-19, according to the democratic press.[2] It was discovered that HCQ is a more potent and safer antiviral drug than CQ.[3] HCQ and CQ have similar chemical structures and act as weak bases and immune modulators.[4] HCQ is crucially cognate with viral burden reduction in COVID-19 patients.[5] It is a chlorinated aminoquinoline that shows wide biological activity, often used as an antimalarial drug.[6] Over the years, HCQ has been used for the treatment of systemic and cutaneous lupus erythematous conditions, chronic Q fever, rheumatoid arthritis, and various skin disorders.[7] In terms of metabolic benefits, HCQ is associated with

*E-mail: jmanjanna@gmail.com

improved lipid profiles, lower blood glucose levels, lower thrombosis rates, retinopathy, hyperpigmentation, and myopathy. During pregnancy, intake of HCQ is safe and mostly used in antibody screening.[8] HCQ inhibits cellular lysosomal functions and improves anticancer,[9] antibacterial, antifungal, and antiviral characteristics.[10] Additionally, it is one of the immune boosters and immune-modulatory drugs. It balances auto-immune diseases by adopting the T-cell subgroup function.[11,12] HCQ could hinder the replication process of coronavirus[13] and it improved the clinical outcome of patients infected by SARS-COV-2.[14] Patients who consume HCQ orally have shown large concentrations in their liver, spleen, kidney and lungs, which are 200–700 times more, concentrated than their plasma and provide an acidic environment that prevents the multiplication of viruses. As a result, it is plausible that the HCQ concentration in the tissues has been reached to prevent SARS-CoV-2 infection. Recent research and articles demonstrated that HCQ reduced SARS-CoV-2 viral activity and inhibited COVID-19 infection in vitro.[15]

On the other hand, water pollution is a major issue facing humanity worldwide. During the period of pandemic, the production and usage of large pharmaceutical products may led to their contamination and/or harmful effects on the environment. HCQ was one of the maximum used/produced drugs for Covid-19. Huge amounts of antiviral drugs can inhibit the extreme growth of microbial required for wastewater treatment.[16] Hospitals, research fields using therapeutic substances, human and animal waste, the release of expired medication into the environment are the main sources of pharmaceutical pollutants in the ecosystem. Hospitals are one of the main sources of drug leakage into the environment.[17,18] Humic acids, NO_3^-, Cl^-, HCO_3^-, Fe^{3+} and other naturally occurring components have a considerable impact on the photodegradation of organic pollutants.[19,20] Pharmaceutical wastewater has been subjected to adsorption, coagulation, sonolysis, and ozonation to extract HCQ. Alternatively, photocatalysis seems to be effective process that is both inexpensive and environmentally benign for removing HCQ.[21] Therefore, removal of HCQ from the soil and aquatic environments is of interest.

Copper oxide nanoparticles (CuO nanoparticles) are interesting materials owing to their stability, non-toxicity, relatively low cost, facile preparation, etc. It has a narrow bandgap of 1.2 eV and is a p-type semiconductor.[22] It is emerging as one of the promising candidates as the active electrode material. The CuO nanostructures exhibit unique characteristics, which are different from their bulk counterparts, and they are used in the development of optical and semiconductor-based sulphide sensors.[23] CuO has been studied as a sensor for hydrogen peroxide.[24] It exhibits good L-cys detection and selectivity[25] and CuO exhibited the best adsorption and adhesion capacity with the substrates, which promotes the transfer of electrons toward the analyte.[26] The CuO has multi-functional properties with encouraging applications such as superconductors, catalysts, solar energy, magnetic storage, gas sensors, photocatalyst, and electrochemical sensors.[27,28] Copper oxide/tin oxide (CuO/SnO_2) is one of the bimetallic electrocatalyst for sensing applications,[29] electrochemical deposition[30] and high-conducting anodes for lithium-ion batteries.[31] The synthesis of CuO nanoparticles by the sol-gel method is more facile and cost-effective.[32] When CuO nanoparticles are in contact with the electrolyte, they possess a sufficient electron charge transfer efficiency.[33]

When compared to bare CuO nanoparticles, the nanocomposite (NC) produced by the combination of CuO and GO have additional benefits, and they improve CuO adsorptive capabilities by expanding its surface area. The synthetic CuO/GO NC serves as an antioxidant, a catalyst (reduction of aromatic nitro compounds), and a non-enzymatic glucose sensor for food.[34] The CuO/GO acts as a photocatalyst for the elimination of methyl red (MR) and as an effective diesel additive.[35] The electrochemical pathway of HCQ sensing involves the oxidation of HCQ by CuO/GO NC. In photocatalytic degradation, light-induced reactive species (mainly OH radicals) are formed to decompose HCQ molecule.

For the quantification of HCQ, analytical techniques like chromatographic, fluorescence, chemiluminescence, and mass spectroscopy have disadvantages such as the need for the pre-treatment of the sample, high consumption of chemicals, and time for analy-

sis, which results in high amounts of waste. The electrochemical approaches are environmental friendly for the detection of target analytes. Therefore, electrochemical techniques have advantage over traditional analytical techniques due to their increased sensitivity, lower cost and fast analysis times.[36)]

Although electrochemical detection of HCQ drug using different electrodes is reported in the literature,[6,14)] there are no reports on the usage of CuO/GO NC/MCPE. We have used this system for the detection of HCQ as well as its photocatalytic degradation. Thus, CuO/GO NC played an excellent role in the two different applications. We showed the detection of HCQ drug at the nM level which is a significantly lower limit when compared to detection limits reported (Table 1).

In this study, the main focus is to synthesize the CuO nanoparticles, GO and CuO/GO NC for the modification of the carbon paste electrode (MCPE). Thus, the CuO/GO NC/MCPE is used as electrochemical sensor in phosphate buffer (PB) solution at pH 7. Different techniques such as cyclic voltammetry (CV) and differential pulse voltammetry (DPV) were used for the detection of HCQ, and photocatalytic degradation of HCQ was examined using CuO/GO NC.

2. Experimental

HCQ tablets were purchased from the pharmacy and used as analytes by dissolving in water (without any further purification). The as-obtained analytical-grade chemicals are used throughout this study. The graphite powder, HNO_3, HCl, H_2SO_4, $KMnO_4$ and H_2O_2 were used in the synthesis of GO. The CuO nanoparticles were prepared using $[Cu(CH_3COO)_2{\cdot}H_2O]$ and L-ascorbic acid. The graphite powder and silicone oil were used as a substrate for the modification of CPE with GO, CuO and CuO/GO NC. PB was prepared using NaH_2PO_4 and Na_2HPO_4. For all the experiments, freshly prepared solutions in distilled water were used.

2.1 Apparatus and electrochemical measurement

Powdered X-ray diffraction patterns were obtained using a Rigaku MiniFlex powder 600 with Cu-K_a radiation (λ_a = 0.154 nm) diffractometer. Thermo Scientific Nicolet-iS5 spectrometer was used to record FT-IR spectra using the KBr pellet method (1 mg of the sample in 300 mg of KBr), TG/DSC was recorded by using TA Instrument SDT Model 650, Using a high-resolution transmission electron microscope (HR-TEM, JEOL JEM F-200) and a field emission scanning electron microscope (FE-SEM, model JEOL JSM-7100F) the morphology of the catalysts was examined. A spectrophotometer (Shimadzu, UV-1800) was used to record the UV-visible spectrum. Photoluminescence spectroscopy (PL) was used to measure the recombination rate. An Auto-Lab (PGSTAT, 204, Netherlands) three-electrode system was used for the electrochemical measurements. The bare CPE, CuO/MCPE, GO/MCPE, and CuO/GO NC/MCPE were used as working electrodes, Ag/AgCl as the reference electrode and the Pt disc as the counter electrode. All the experiments were conducted at room temperature (RT, ~27 ºC).

2.2 Synthesis of graphene oxide

The modified Hummer's method[37)] was used here to prepare the GO. Accordingly, about 3 g of graphite powder was taken in a round bottom flask with mixture of 25 mL each of HNO_3 and H_2SO_4 was added in it. To this, $KMnO_4$ (3 g) was added slowly with stirring for two hours, the suspension was agitated in an ice-cold environment. Then, it was brought to room temperature and about 200 mL of warm distilled water was added with 4 h of continuous stirring. 10 mL of H_2O_2 (30 vol.%) was added carefully (drop-wise) and diluted with hot water. The solid product was separated by centrifugation. To get rid of the sulphate ions, it was repeatedly rinsed with a 5 vol.% HCl solution and then distilled water. To form a stable GO dispersion, the cleaned GO was eventually dissolved in water using an ultrasonic bath and then dried for 6 h in a hot air oven at 80 ºC.

2.3 Synthesis of copper oxide nanoparticles

A 500 mL (0.1 M) cupric acetate monohydrate solution received approximately 100 mL (0.2 M) of L-ascorbic acid in an aqueous solution while being continuously stirred on a magnetic stirrer for about

30 minutes at room temperature. The solution's colour changed from blue to reddish-brown quickly as metallic copper formed, indicating a rapid reduction process of cuprous oxide (Cu/Cu_2O) particles. The final product was filtered and washed with distilled water followed by a drying period of 4 h in a hot air oven at 80 °C. The final red powder was thoroughly ground to a fine powder and annealed at 600 °C for approximately 5 h to get the entirely oxidized black-coloured product, CuO.

2.4 Synthesis of CuO/GO NC

1 g of GO and 0.5 g of CuO were taken in 50 mL of water kept in stirred condition. To this, 100 mL of 0.1 M NaOH solution was added slowly and kept stirred continuously for about 4 h at 100 °C. The solution was cooled to room temperature, and centrifuged at 6000 rpm. The final product was separated, washed with distilled water and ethanol, and then dried at 60 °C in an oven for about 6 h.

2.5 Modification of carbon paste electrode (Sensor)

Before modification, the carbon paste electrode (CPE) was cleaned thoroughly using distilled water in an ultrasonic bath. In an agate mortar, 1.0 g of graphite powder and 0.5 mL of silicone oil were combined and pulverized. The end of a Teflon tube's hollow was filled with this homogeneous paste. A copper wire attached to the paste in the tube's inner hole provided the electrical contact, which has a geometrical surface area of 0.08 cm^2. Further, the MCPE was prepared with CuO, GO and CuO/GO NC. The MCPE is indicated as CuO/MCPE, GO/MCPE and CuO/GO NC/MCPE.

2.6 Photo catalytic experiment

In a typical experiment, 100 mL of HCQ solution and 20 mg of the catalyst (*i.e.*, CuO, GO and CuO/GO NC) were taken and kept stirred under visible light. A UV-Vis spectrophotometer was used to assess the change in HCQ concentration (*i.e.*, absorption intensity) by collecting sample through syringe filter at different intervals. The photocatalytic degradation efficiency was determined.[38] After the photodegradation studies, the photocatalyst was collected back by centrifugation and cleaned with alcohol and dried for the reusability test.

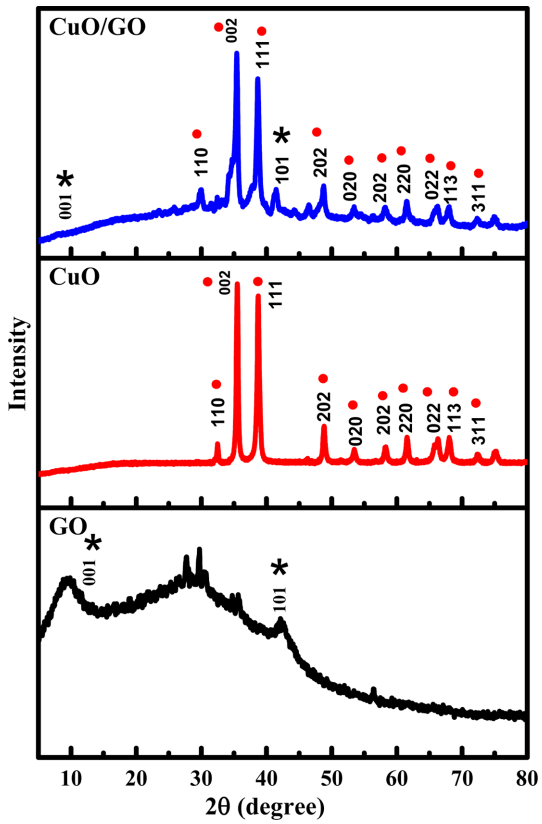

Fig. 1. XRD patterns of GO, CuO, and CuO/GO NC.

3. Results and Discussion

3.1 Structural analysis of CuO/GO NC

Fig. 1 is the XRD patterns of GO, CuO and CuO/GO NC. The (001) and (101) planes of GO are seen at 2θ = 10.02° and 42.23°, which matches with JCPDS No. 75-1621. The peak at 10.02° confirms the formation of GO by the Hummer's method through the oxidation of graphite.[39,40] The XRD peaks of CuO could be indexed to monoclinic structure with a space group of (C 1 2/c 1), and matched with COD entry number 96-721-2243[41] as shown in Fig. S1 along with matching report from MATCH!. The lattice parameters found to be a = 4.6837 Å, b = 3.4226 Å, c = 5.1288 Å. There are no additional peaks found, which indicates the formation of CuO here.[42] The GO peaks are marked (*) in CuO/GO NC.

It is presumed that the carbonyl groups of car-

boxylic acids and ketones present on GO are associated with the Cu (II) of CuO that create a layer-on-layer network. Thus, hydrophilicity of CuO/GO NC is expected to increase due to porous 3D network.[34] Fig. S2 shows the XRD pattern of HCQ. The sharp and intense diffraction peaks here indicate the crystalline nature.

The Scherer equation was used to determine the average crystallite size, $(D) = 0.9\lambda/\beta\cos\theta$ where l = 0.154 nm, wavelength of Cu K_a line and is the FWHM in radians of the 100% peak in the XRD pattern. Accordingly, D of CuO, GO and CuO/GO NC are found to be 47.9 nm, 1.69 nm and 8.45 nm, correspondingly.

3.2 FTIR spectra of CuO/GO NC

The FT-IR spectra of GO, CuO and CuO/GO NC are depicted in Fig. 2. In the FTIR spectra of GO, the oxygen functionalities present at 3408 cm^{-1} are equivalent to the stretching vibration of –OH. The –CH symmetric and asymmetric stretching is seen at 2921 cm^{-1} and 2853 cm^{-1}, respectively. The peaks at 1626 cm^{-1} is assigned to the stretching vibration of –C=C. The stretching and bending vibrations of epoxy group (C–O–C) are seen at 1384 cm^{-1} and 1122 cm^{-1}. The C–O and –C=C groups found here confirm the oxidation of graphite to GO. In the case of CuO nanoparticles, symmetric and asymmetric stretching of O–H bond (due to adsorbed moisture) are seen at 3446 cm^{-1}, 2932 cm^{-1} and bending vibration at 2866 cm^{-1}. A strong peak around 530 cm^{-1} corresponds to Cu–O stretching of monoclinic CuO.[43,44] In the IR spectra of CuO/GO NC, there are no bands for C=O as GO is associated/ conjugated with CuO. The peak at 1400 cm^{-1} is from carbonyl group C–O and it showed more intense than in GO and CuO. Strong and sharp IR peaks at 571 and 522 cm^{-1} are attributed to the stretching caused by the Cu–O bond, which had slightly displaced from 533 cm^{-1} and indicated the presence of the Cu–O bond. Thus, FTIR spectra confirm the synthesis of CuO/GO NC. Fig. S3 indicates the FTIR spectra of HCQ. The broadband of –O–H stretching vibration was observed at 3421 cm^{-1}. A small peak at 2923 cm^{-1} was attributed to –C–H stretching vibration. The two peaks at 1617 and 1558 cm^{-1} correspond to the –C=C stretching vibration of an aromatic ring. A sharp peaks at 1054 and 1124 cm^{-1} are due to –C–Cl and –C–N stretching vibrations, respectively. The IR bands observed here for HCQ matches with the earlier study.[45]

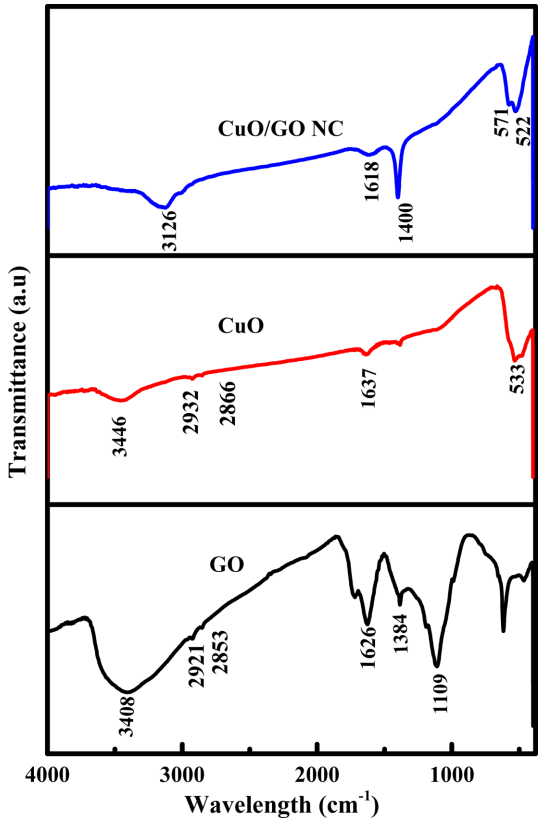

Fig. 2. FTIR spectra of GO, CuO, and CuO/GO NC.

3.3 Thermal analysis of CuO/GO NC

The TG/DSC plots provide structural details and thermal stability of composite material here. If there are any impurities, the nature of the TG/DSC would be different from the expected behavior. Fig. 3 shows TG/DSC plots of GO, CuO and CuO/GO NC recorded at a scan rate of 4 °C min^{-1} under ambient condition. In the case of GO, about 7% weight loss occurred below 150 °C owing to the elimination of surface adsorbed water. Thereafter, about 20% weight loss was observed up to 700 °C due to loss of labile oxygen-containing functional groups.[46,47] The resultant DSC curve in Fig. 3a shows the decomposition of GO at 220 °C. In the case of CuO, as shown in Fig. 3b, it is stable up to 700 °C. A negligi-

ble weight loss of 0.7% was observed due to the loss of surface bound water. The TGA curve of CuO/GO NC is shown in Fig. 3c, and the weight loss around 120 °C is due to the removal of adsorbed water. The second degradation stage begins around 300 °C and ends at 500 °C. In this temperature, GO layers are stable. The gradual weight loss in the 600–700 °C range is due to the depletion of more stable oxygen functions. Additionally, the DSC plot shows two endothermic peaks at 177 °C and 691 °C. Fig. S4 depicts the TG/DSC of HCQ. A weight loss of about 2% was seen between 150 to 200 °C. A major weight loss of about 30% was observed between 240 and 300 °C. About 23% of weight loss was observed between 300 to 700 °C. Similar thermal behaviour was reported for HCQ in the earlier report.[48)]

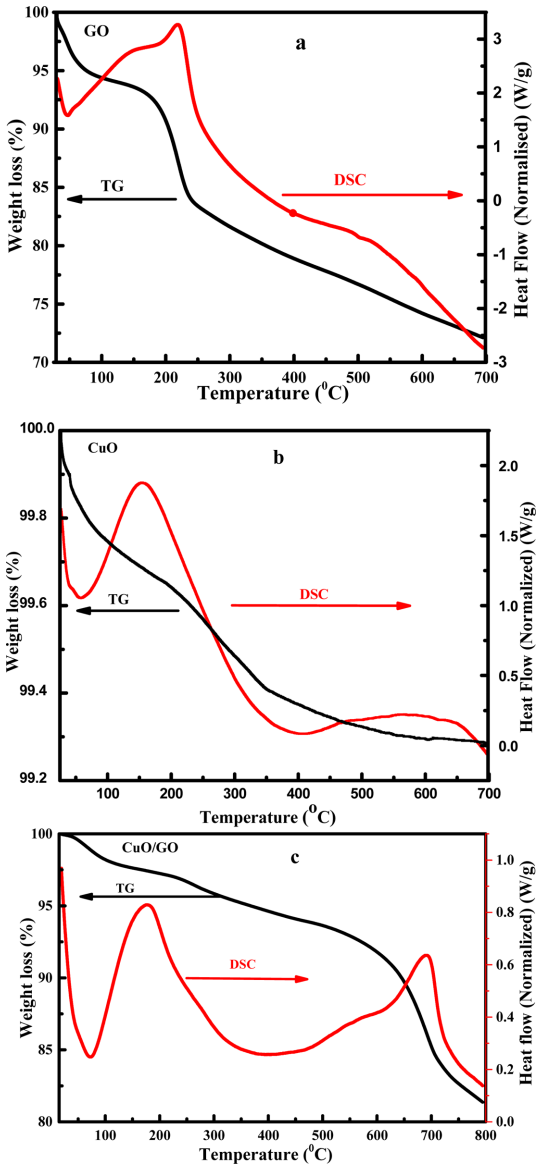

Fig. 3. TG/DSC plots of (a) GO, (b) CuO, and (c) CuO/GO NC.

3.4 Morphological analysis of CuO/GO NC

Fig. 4 shows the FESEM image of GO, CuO and CuO/GO NC. The GO shows wavy, wrinkled and layered morphology whereas CuO and CuO/GO NC show polydispersed (irregular size and shape) morphology. As shown in the TEM image, the sizes of CuO/GO NC are in the range of 10–50 nm but in agglomerated form. The ring pattern of bright spots in the selected area electron diffraction (SAED) indicates the single crystalline nature. However, the axial orientation in a single crystal has random directions.[49–51)]

3.5 UV-Vis spectra of GO, CuO, and CuO/GO NC

The UV-Vis spectra of GO, CuO and CuO/GO NC are shown in Fig. 5a. The CuO/GO NC exhib-

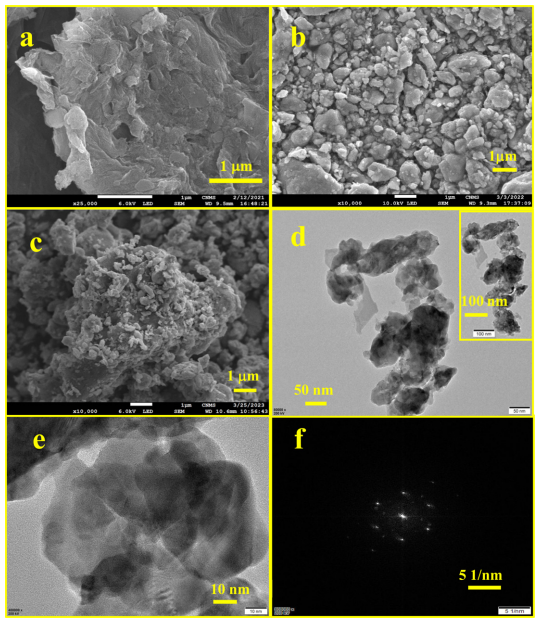

Fig. 4. SEM images of (a) GO, (b) CuO and (c) CuO/GO NC. (d,e) TEM images and (f) SAED pattern of CuO/GO NC.

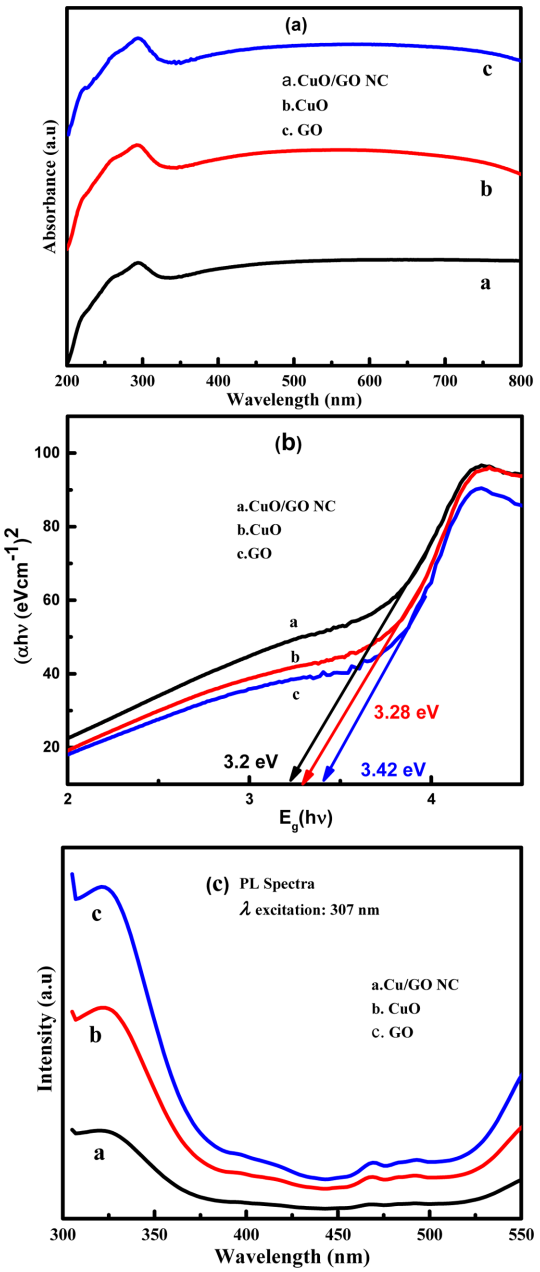

Fig. 5. (a) UV-visible spectra, (b) Tauc's plot, and (c) Photoluminescence spectrum of GO, CuO and CuO/GO NC.

its a relatively higher absorption around 290 nm when compared to GO and CuO. Tauc's equation, $(ahv)^{1/n} = A\ (hv - E_g)$ was used to get the band gap value, where a is the absorption coefficient (a = 2.3030 (A)/t, where t is the sample thickness.), h is the Planks constant (6.626×10^{-34} J·s), v is the photons frequency, A is the proportionality constant, and E_g is the band gap energy (n = ½ and 2 for direct and indirect band gap). The direct bandgap was obtained here by plotting $(ahv)^2$ *vs.* hν as illustrated in Fig. 5b. Thus, the band gap of GO, CuO and CuO/GO NC were found to be 3.42, 3.28, and 3.20 eV, respectively, whereas E_g of bulk GO (around 2.2 eV) and CuO (around 1.2 eV) are well known. The higher bandgap value indicates the formation of nanostructure here.

3.6 Photoluminescence (PL) spectra

The charge separation and recombination process of photogenerated electrons and holes is a crucial aspect of photocatalytic activity. Examining the photoluminescence (PL) spectra of the as-prepared samples reveals the catalytic activity of the samples. The photo catalytic activity is enhanced by limiting the recombination of photoinduced electrons and holes. On the CuO and GO surface, oxygen sites and defects are produced. Fig. 5c is the PL spectra of GO, CuO and CuO/GO NC in water at room temperature, with an excitation wavelength of 307 nm. The emission peaks are seen at 324, 323 and 320 nm for GO, CuO and CuO/GO NC, respectively. When compared to GO and CuO, the emission intensity of CuO/GO NC is reduced, which indicates the increased e^-–h^+ migration and lower recombination.[52] Thus, CuO/GO NC is expected to provide increased photocatalytic efficiency for drug degradation.

3.7 Electrochemical behaviour of MCPE

Fig. 6(a) shows the cyclic voltamogram (CV) for 5 mM $[Fe(CN)_6]^{3-/4-}$ in 0.1 M KCl using different working electrodes. Both oxidative (anodic) and reductive (cathodic) peaks are seen for this reversible one electron transfer system. The current obtained with CuO/GO NC/MCPE increased significantly when compared to bare CPE, GO/MCPE and CuO/MCPE. This indicates the advantage of composite electrode due to higher electron transfer and/or increased electronic conductivity. Fig. 6b shows Nyquist plot for the same system with Randles equivalent circuits to analyze the electron transmis-

sion (R_{ct}) performance. The semi-circular component at lower frequency is related to the diffusion process, and a linear portion at higher frequency is related to the electron transfer restricted process. The R_{ct} for bare CPE, CuO/MCPE, GO/MCPE and CuO/GO NC/MCPE were found to be 18908 W, 15413 W, 9227 W and 8597 W, respectively. Decrease in the R_{ct} value indicate the increase of electron transfer rate. Thus, the presence of the CuO/GO NC enabled more efficient electron transfer between the solution and the electrode surface.

As per Randles-Sevcik equation, $I_{pa} = (2.69 \times 10^5)\ AD^{1/2}\ n^{3/2}\ n^{1/2}\ C$ where n is the number of electrons exchanged, A is the surface area of the electrode (cm^2), C is the concentration (mol cm^{-3}), D is the diffusion coefficient ($cm^2\ s^{-1}$) and n is the scan rate ($V\ s^{-1}$). The linear behaviour is seen for plot of I_{pa} *vs.* $n^{1/2}$ which indicates fast electron transfer reactions with CuO/GO NC/MCPE. Surface area A of the MCPE here are 0.067, 0.083, 0.85 and 0.90 cm^2 for the bare, CuO, GO and CuO/GO NC respectively. In comparison to a bare electrode, the CuO/GO NC shows higher A and hence adsorption of analyte is expected to be higher on its surface to facilitate redox reactions.

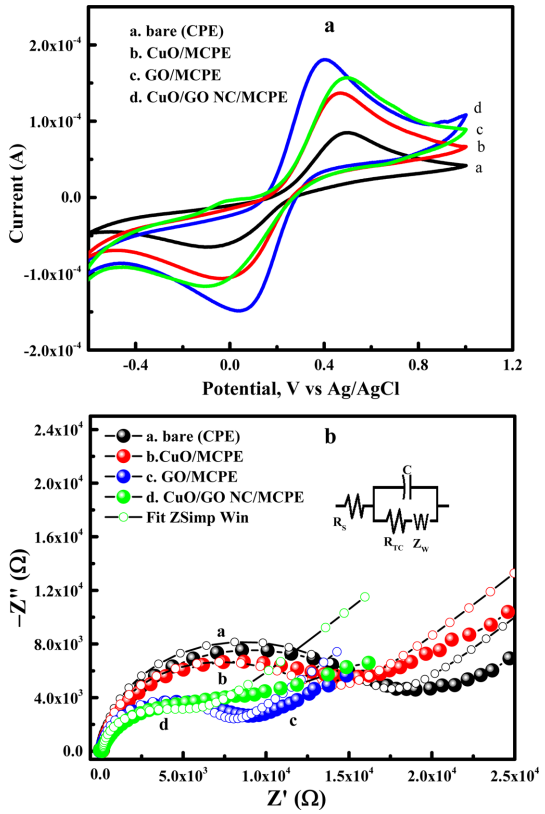

Fig. 6. (a) CVs and (b) Nyquist plot using bare (CPE), CuO/MCPE, GO/MCPE and CuO/GO NC/MCPE for 5 mM $[Fe(CN)_6]^{3-/4-}$ in 0.1 M KCl.

3.8 Electrochemical response of HCQ using modified electrodes

Electrochemical detection of HCQ in 0.1 M phosphate buffer (pH 7) was done in a conventional three-electrode arrangement with bare (CPE), GO/MCPE, CuO/MCPE and CuO/GO NC/MCPE as a working electrode. As shown in cyclic voltammetric behaviour of HCQ (Fig. 7), high current is observed for the oxidation of HCQ using CuO/GO NC/MCPE, unlike other electrodes here. The nanocomposite of GO and CuO can lead to a synergistic effect in terms of electrocatalytic activity. The presence of both materials may enhance the efficient catalytic reaction for HCQ, leading to improved current. HCQ is expected to be neutral species at pH 7 and hence its interaction with CuO/GO NC/MCPE is enhanced through catalytic activity. HCQ shows two oxidation peaks: the first peak around 0.77 V with an Ipa of 9.1×10^{-6} µA is due to deprotonation of –OH group and the second around 0.99 V with a Ipa of 1.7×10^{-5} µA is due

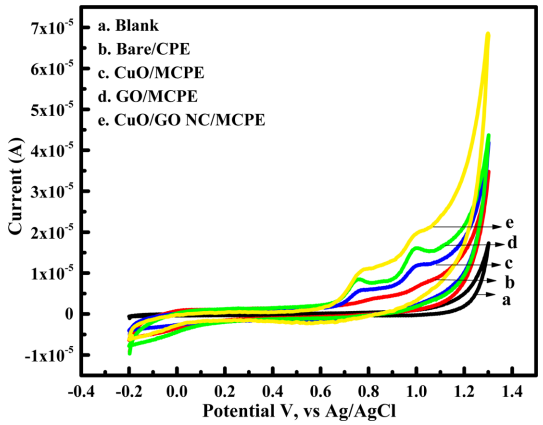

Fig. 7. Cyclic voltammograms of 1 mM HCQ in phosphate buffer (pH 7): (a) Blank, (b) bare CPE, (c) CuO/MCPE, (d) GO/MCPE and (e) CuO/GO NC/MCPE with HCQ; Accumulation time 30 sec.

to deprotonation from primary carbon atom for conversion to aldehyde,[53] as shown in Fig. S5. It is an irreversible reaction as there is no cathodic peak/s during the reverse scan.

3.8.1 Effect of catalyst dose on oxidation of HCQ

The CV of HCQ on varying dose of CuO/GO NC was examined to optimize the catalyst concentration. The maximum anodic peak current (I_{pa}) was obtained at 50 mg of catalyst due to increase in active sites as shown in Fig. S6, a plot of CuO/GO NC dose *vs.* peak current. At higher catalyst appropriate homogeneity is hindered thereby active sites are less available. Thus, 50 mg of CuO/GO NC was used here for further investigation.

3.8.2 Effect of accumulation time of HCQ

The peak current response to HCQ adsorption on the electrode surface can be understood by determining the accumulation time, as shown in Fig. S7. The maximum peak current was obtained at an accumulation time of 30 s. At longer accumulation time (> 30 s), there occurs an adsorptive equilibrium of HCQ on the modified electrode surface leading to decrease in charge transfer.[54] Thus, ideal accumulation time of 30 s was used throughout this study.

3.8.3 Effect of pH

The optimum pH for detection of HCQ is determined here by varying pH from 4.0 to 11.0 at a scan rate of 100 mV s^{-1} by recording CV as shown in Fig. 8a (pH 4 to 7) and Fig. 8b (pH 8 to 11). It is clear that Ipa increased with increase in pH up to pH 7 and thereafter, Ipa decreased (Fig. 8c). This behavior is typical of electrode process, wherein appearance of possible acid/base equilibrium is indicated by the protonic concentration of the solution (pH ≤ 7). When a pH is raised (> 7) to a point where almost no acid is

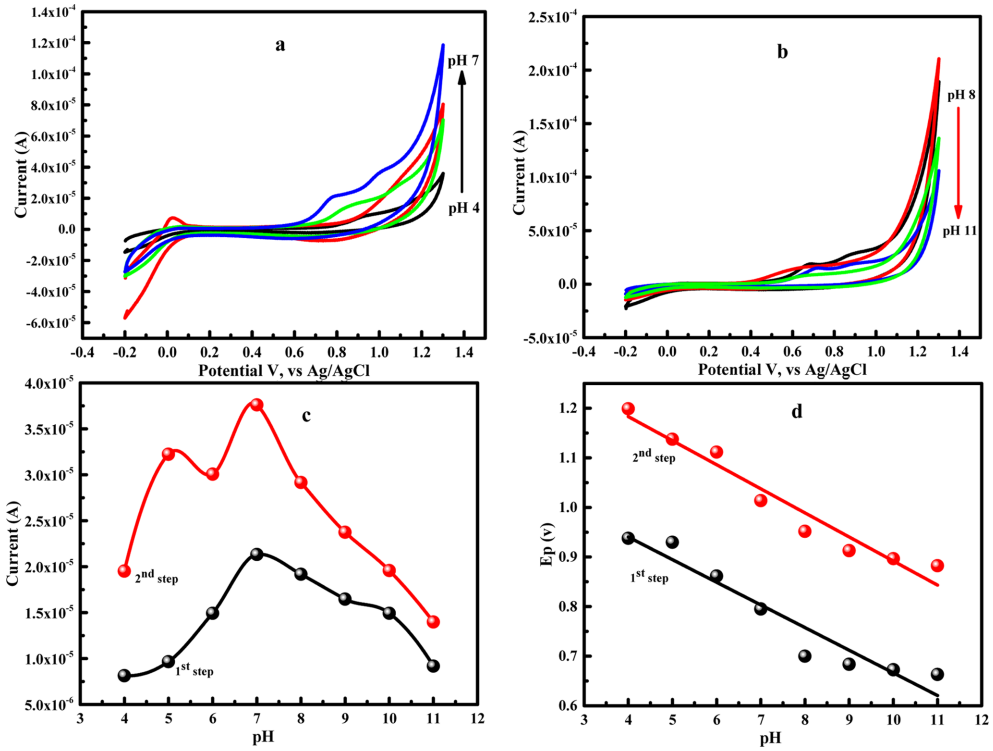

Fig. 8. (a,b) Effect of pH on the shape of the anodic peak in the presence of 1 mM HCQ at different pH. (c,d) The first line (black/1st step) and second line (red/ 2nd step) indicates the relationship between the peak current (I_{pa}) and peak potential (E_p) *vs.* pH, respectively, for the two-step oxidation process of HCQ.

formed and conjugate bases can undergo reduction, typically at higher negative potentials, the rate of such de-protonation rises.[53] Thus, pH 7 is the optimised pH for all the measurements here. Furthermore, Fig. 8d is the E_p *vs.* pH which follow linear equation Ep (V) = –0.0456 + 1.1230 pH; R^2 = 0.92 for first peak and E_p (V) = –0.0485 +1.3773 pH; R^2 = 0.95 for second peak. As the pH of the solution increased, the peak potential changed towards a less positive value, showing that protons are involved in the electrode action, as seen from the plot of E_p against pH. Based on the slope of E_p *versus* pH, it is revealed that there are equal number of protons and electrons present, which is related with earlier report.[55] HCQ is in its negatively charged state at pH 7, which may increase the electrode surface and lead to a greater peak current at pH 7, despite the pH being optimal for biological fluids.

3.8.4 Effect of scan rate

CV of HCQ was recorded at pH 7 with different scan rates (20 to 120 mV s^{-1}) as shown in **Fig. 9a**. The I_{pa} increased linearly with increase in scan rate as depicted in Fig. 9b, I_{pa} *vs.* $\nu^{1/2}$ which follows I_{pa} = 4.1532 $\nu^{1/2}$ – 1.8339 (R^2 = 0.91) for first peak and I_{pa} = 7.2569 $\nu^{1/2}$ – 3.1371 (R^2 = 0.92). The relationship between the slope of the logarithm of the peak current *vs.* the logarithm of the scan rate is plotted in Fig. 9c. The derived linear correlation is obtained as log I_{pa} =1.2625 log ν – 7.1796; R^2 = 0.98 for first peak and log I_{pa} =1.239 log ν – 6.8768; R^2 = 0.99 for second peak. Based on the slope obtained here, the electrode reaction is presumed to be adsorption-controlled.[56] Further, as shown in Fig. 9d, linear relationship is seen for E_{pa} *vs.* log of scan rate, and the corresponding equation is E_{pa} (V) = 0.06462 log ν + 0.6475 (R^2 = 0.82) for first peak and E_{pa} (V) = 0.00134 log ν +

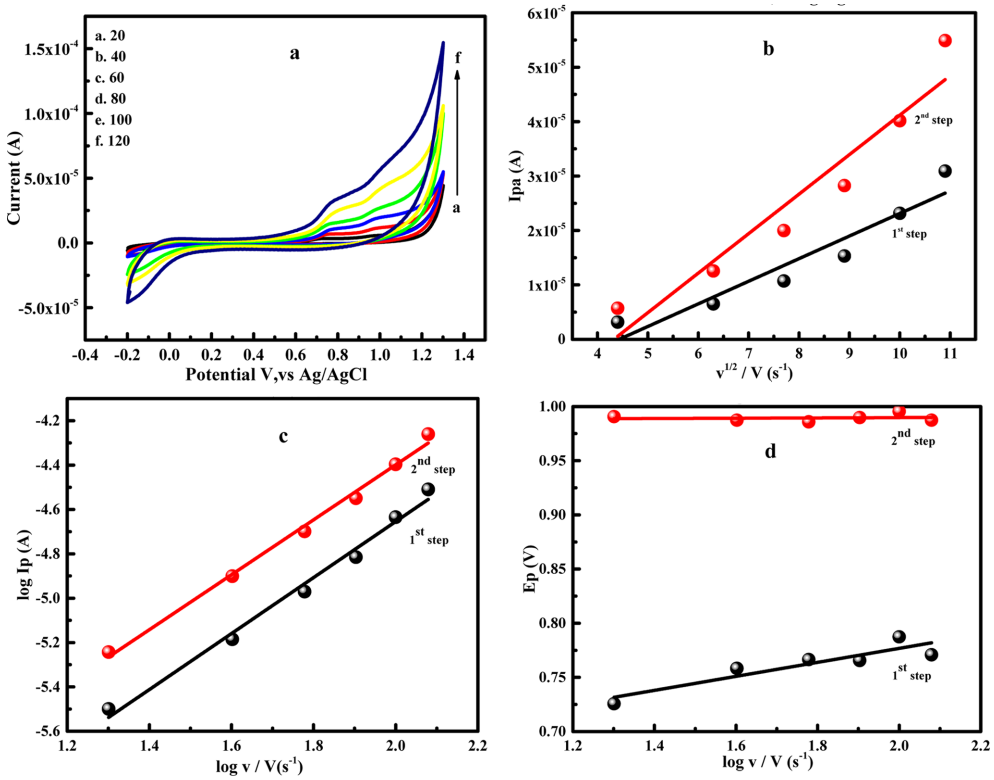

Fig. 9. (a) CVs of 1 mM HCQ at various scan rates (20 to 120 mV s^{-1}). (b–d) The first line (black; 1st step) and second line (red; 2nd step) indicates the relationship between the (b) I_{pa} *vs.* $\nu^{1/2}$, (c) log I_{pa} *vs.* log *v*, and (d) E_p *vs.* log *v*, respectively for the two-step oxidation process of HCQ.

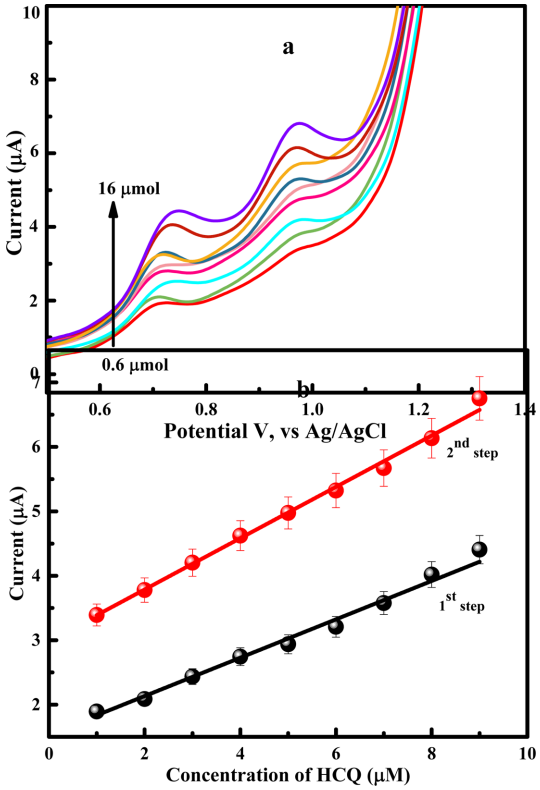

Fig. 10. (a) DPV of HCQ with various concentrations of HCQ ranging from 0.6 to 16 µM obtained at CuO/GO NC/MCPE in pH 7 PB (n=3). (b) The first line (black; 1st step) and second line (red; 2nd step) indicates the relationship between the peak current (I_{pa}) *vs.* concentration of HCQ for the two-step oxidation process of HCQ.

0.9870 (R^2 = 0.01) for second peak.

Laviron equation was used to calculate the heterogeneous rate constant (k_o) and number of electrons transported (n) for the irreversible electrode process.[57)]

$$Epa = E^o + (2.303\ RT/\alpha\ nF)\ \log\ (RT\ k_o/\alpha\ n\ F) + (2.303\ RT/\alpha\ nF)\ \log\ \nu$$

The n = 1.79 (*i.e.* ~2) is obtained here from the slope of the E_{pa} *vs.* log scan rate plot. Therefore, two protons and two electrons will be transported during HCQ oxidation,[53,58–60)] Fig. S7. The charge transfer coefficient (α) value for the irreversible process was about 0.5. The intercept value of the

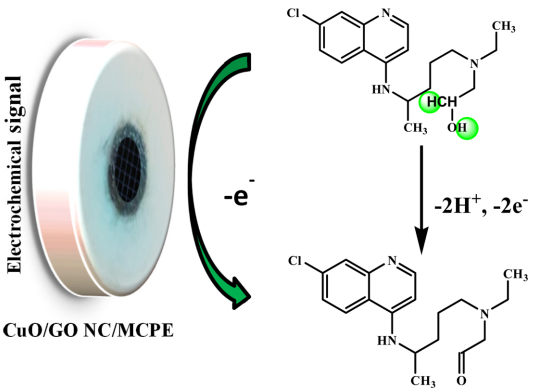

Fig. 11. Schematic representation of plausible mechanism for electro oxidation of HCQ on CuO/GO NC/MCPE.

E_p *vs.* n plot can be used to calculate the value of (E^o) by inducing it to the vertical axis at ν = 0. In this case, E^o and k_o were determined to be 0.7311 and 1.5891, respectively.

Differential pulse voltammetry (DPV) is used here for detection threshold and sensitivity of HCQ using CuO/GO NC/MCPE as working electrode. Fig. 10a is the DPV for different concentration (0.6 µM to 16 µM) of analyte, HCQ. The peak current increased linearly with increase in HCQ concentration (**Fig. 10b**), the equation for linear regression is Ipa(mA) = 0.2978 [HCQ] (mM) + 1.5371 (R^2 = 0.98) for first peak and Ipa(mA) = 0.3982 [HCQ] (mM) + 2.9898 (R^2 = 0.99) for second peak. We have determined the relative sensitivity (= slope/area) and LOD (= 3 × SB/S) where S is the slope of the calibration curve and SB is the standard deviation of three measurements made from the signal acquired from the blank. The 3 is a result for 90% confidence level in the distinction between the observed signal and the blank.[61)] The sensitivity was found to be 0.3 to 0.4 µA μM^{-1} cm^{-2} and LOD was found to be 69 to 92 nM. The relatively high sensitivity for HCQ with CuO/GO NC/MCPE is ascribed to its good electro-catalytic activity and enhanced surface area which enables rapid transfer of electrons during oxidation of HCQ with increasing active sites or connected structures of the electrode.[62–64)] As a result, the peak current in CV and DPV is ascribed to irreversible oxidation of OH group in HCQ to –CHO. Fig. 11 is the

Table 1. Comparison of the detection of HCQ using different modified electrodes

Electrode Material	Supporting Electrolyte	Technique	Sample	Linear range	LOD	Ref
GCE	BR	DPV	HCQ	2×10^{-5} to 4×10^{-6}	112 nM	[6]
SDSMCNTPE	PBS	CV	HCQ	10×10^{-6} to 40×10^{-6}	850 nM	[55]
GCE/VS_2QDs	BR	DPV	HCQ	0.84–22.5×10^{-8}	277 nM	[59]
GrRAC	H_2SO_4	DPV	HCQ	5×10^{-6} to 65×10^{-6}	1050 nM	[60]
ZnO@CPE	PBS	SWV	HCQ	1×10^{-3} to 0.8×10^{-3}	1331 nM	[65]
3D-CB/PLA	BR	SWV	HCQ	0.4×10^{-6} to 7.5×10^{-6}	40 nM	[66]
CuO/GO NC/MCPE	PB	DPV	HCQ	0.6×10^{-6} to 16×10^{-6}	69 nM	Present work

GCE: Glassy carbon electrode; CPE: Carbon paste electrode; SDSMCNTPE: Sodium dodecyl sulphate modified carbon nanotube paste electrode, VS_2QDs: Vanadium sulphide quantum dots; GrRAC: Cork graphite sensor; ZnO@CPE: Zinc oxide carbon paste electrode; 3D-CB/PLA: 3D-printed CB-PLA electrode. BR: Britton Robinson buffer; PBS: Phosphate buffer saline; H_2SO_4 as electrolyte, PB: Phosphate buffer.

schematic representation of the electrode process involved in the oxidation of HCQ. As shown in Table 1, LOD and linear range values obtained here for HCQ are compared with previous reports.[65,66]

3.8.5 Stability and reproducibility of CuO/GO NC/MCPE

In order to ensure the reproducibility of the electrode surface, CV data from the four cycles for 1 mM HCQ using freshly prepared CuO/GO NC was compared. It was found that the modified electrode retained Ip up to 97%. Furthermore, when the freshly prepared CuO/GO NC electrode was kept for different interval of time before its use, only about 2 to 3% of the current is decreased after 4 h. This demonstrates the reasonable stability and reproducibility of the modified electrode here.

3.9 Photodegradation of HCQ

Fig. 12 shows the UV–Visible spectra of HCQ (0.1 ppm) before and after irradiation under visible light by adding GO, CuO and CuO/GO NC samples. The amount of HCQ degradation was determined based on the calibration curve (absorbance at l = 342 nm *vs*. concentration) by using $(1 - C_t/C_o) \times 100$ where C_0 is the initial concentration of HCQ and C_t is the concentration at different interval of irradiation time.

The maximum degradation (93%) occurred with CuO/GO NC under visible light irradiation for about 34 min. The GO and CuO showed 73% and 3% degradation of HCQ, respectively, under the same experimental conditions. The poor degradation with CuO may be due to the drawbacks of monophasic catalyst and quick recombination of photo-generated charge carriers. On the other hand, the maximum efficiency with CuO/GO NC is due to efficient charge carrier migration between heterojunctions, and decrease in recombination rate.[67,68]

Fig. S8 shows the CuO/GO NC catalyst dose (5–25 mg/100 mL) *vs.* photodegradation efficiency. The catalyst dose must be sufficient to generate electron-hole pairs at a certain rate and generate favourably OH radicals. The % degradation increased marginally as the catalyst dose increased from 5 to 20 mg due to the increase in active sites (point of saturation limit is reached even at 5 mg). Thereafter (*i.e.*, active regions have already been fully used), degradation decreased as a result of the increased turbidity. Consequently, fewer photocatalysts are activated with increased light scattering and lower photon penetration depth.[69] The % photodegradation with 5, 10, 15, 20 and 25 mg of catalyst was 96.33, 96.58, 96.81, 97.07, and 96.93%, respectively, in about 34 min under visible light. As shown in Fig. S8b, % degradation of HCQ increased with irradiation time.

3.9.3 Effect of pH on degradation of HCQ

Fig. S9 shows % degradation of HCQ (0.1 ppm) at different pH with a catalyst dose of 20 mg/100 mL under visible light irradiation for 34 min.

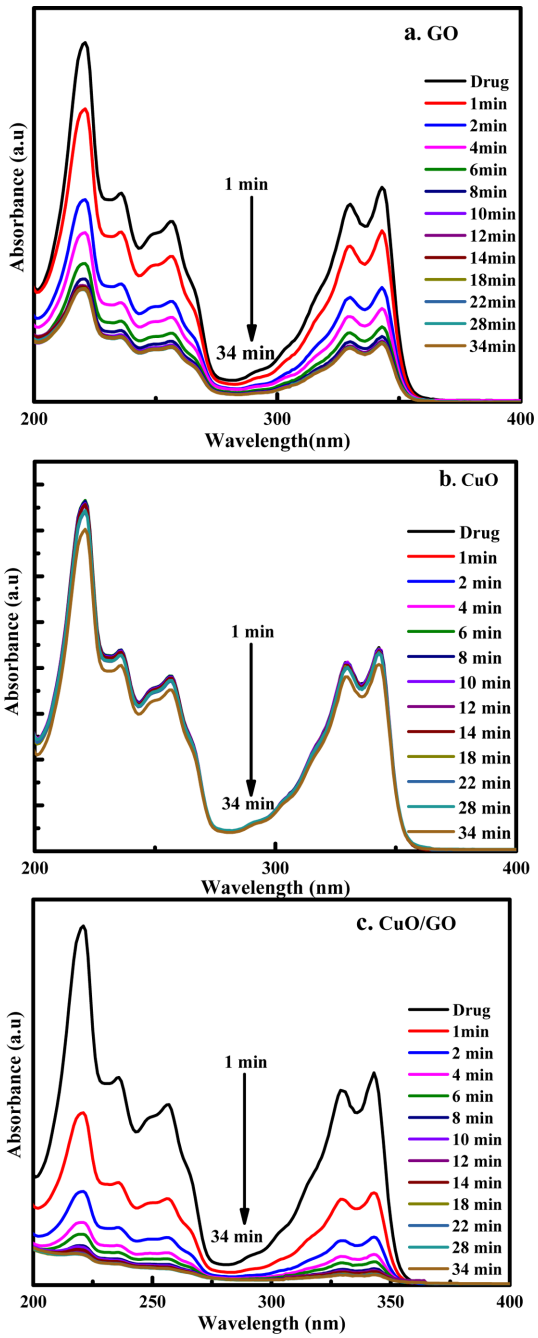

Fig. 12. UV-Visible spectra of HCQ (0.1 ppm) before and after irradiation under visible light by adding (a) GO, (b) CuO and (c) CuO/GO NC samples.

The % degradation increased with increase in pH up to 9 and thereafter decreases significantly. Fig. 9b is the % degradation *vs.* irradiation time in different pH conditions. Due to biological stability of HCQ over a wide pH range, the degradation varies slightly with increasing pH. There is no information in the literature concerning the effect of pH on HCQ degradation. The photocatalysis process is affected by many factors such as semiconductor surface, the generation of OH radicals, presence of electrostatic forces, etc. These process accounts for the enhanced degradation efficiency here at pH 9. At higher pH (above pH > 9), there is a repulsion between the catalyst surface and the contaminant molecule, which slows down the rate of OH radical formation.[52,70] The photodegradation efficiency obtained at pH 3, 5, 7, 9 and 11 are 93.28, 96.29, 98.07, 98.15, and 70.64%, respectively. We have not analyzed the nature of HCQ degradation products, unlike the previous reports.[71,72] Desethylhydroxychloroquine and desethylchloroquine are the main byproducts of HCQ, and they are less potent and have less harmful effects to human beings.

3.9.4 Reusability of catalyst

The optimal photodegradation conditions (0.1 ppm HCQ, 20 mg of CuO/GO NC, pH 9, irradiation under visible light) have been evaluated for catalyst reuse. The catalyst was cleaned, rinsed, and dried at 60 °C for 24 h after each cycle to remove impurities before being placed to use again to check for chemical stability. Fig. S10 shows that the catalyst efficiency is marginally reduced by about 3% in comparison with initial results and 1st cycle. However, after the 4th cycle, the photocatalytic activity decreased by about 11% indicating adsorption of degradation or foreign products and/or surface poisoning, which prevents exposure to active sites. Additionally, CuO/GO NC structural stability is confirmed by comparing the XRD patterns (Fig. S11). It is clear that the pattern remained same except decrease in the intensities of the characteristic peaks related to crystallinity.

4. Conclusions

The highly sensitive CuO/GO NC/MCPE was developed for detecting antimalarial drug (HCQ), which was used for COVID-19 patients during the initial stages. Sensitive MCPE is developed here by

using the techniques CV and DPV. The CuO/GO NC facilitates the rapid transfer of electrons to the oxidation of HCQ. The sensitivity was found to be 0.33 to 0.44 μA μM cm^{-2} and LOD was 69 to 92 nM for CuO/GO NC/MCPE. Thus, CuO/GO NC/MCPE is highly sensitive toward the detection of HCQ. The CuO/GO NC had a photocatalytic degradation efficiency of about 98% (for 0.1 ppm with 20 mg catalyst at pH 9) in 34 min for HCQ, based on UV-visible spectra; the recycle photocatalytic degradation of the HCQ demonstrated the high degree of reusability of CuO/GO NC.

Supplementary Information (SI)

The characterization of XRD MATCH! For CuO/GO,HCQ by XRD, FTIR, TG/DSC, reaction mechanism, catalyst dose, accumulation time, % degradation of HCQ (0.1 ppm) *vs.* catalyst dose, % degradation of HCQ (0.1 ppm) *vs.* pH, stability and XRD of fresh and recovered CuO/GO NC (**Fig. S1–S11**) are provided as supplementary information.

Conflict of Interest

The authors declare that they have no known competing financial interests or personal relationships that could have appeared to influence the work reported in this paper.

Acknowledgments

GSS greatly acknowledges RCU for providing Fellowship under SC/ST grant. Authors have benefitted from the facilities established under DST-FIST (SR/FST/CSI-273/2016 C), Ministry of Science & Technology, Govt. of India & VGST-CESEM (KSTePS/VGST/CESEM/2018-19/GRD No. 746), Govt. of Karnataka, India.

References

1. A. K. Singh, A. Singh, A. Shaikh, R. Singh, and A. Misra, Chloroquine and hydroxychloroquine in the treatment of COVID-19 with or without diabetes: A systematic search and a narrative review with a special reference to India and other developing countries, *Diabetes Metab. Syndr. Clin. Res. Rev.*, **14(3)**, 241–246 (2020).
2. K. A. Pastick, E. C. Okafor, F. Wang, S. M. Lofgren, C. P. Skipper, M. R. Nicol, M. F. Pullen, R. Rajasingham, E. G. McDonald, T. C. Lee, I. S. Schwartz, L. E. Kelly, S. A. Lother, O. Mitjà, E. Letang, M. Abassi, and D. R. Boulware, Review: Hydroxychloroquine and chloroquine for treatment of SARS-CoV-2 (COVID-19), *Open Forum Infect. Dis.*, **7(4)**, ofaa130 (2020).
3. J. Geleris, Y. Sun, J. Platt, J. Zucker, M. Baldwin, G. Hripcsak, A. Labella, D. K. Manson, C. Kubin, R. G. Barr, M. E. Sobieszczyk, and N. W. Schluger, Observational study of hydroxychloroquine in hospitalized patients with Covid-19, *N. Engl. J. Med.*, **382**, 2411–2418 (2020).
4. J. Liu, R. Cao, M. Xu, X. Wang, H. Zhang, H. Hu, Y. Li, Z. Hu, W. Zhong, and M. Wang, Hydroxychloroquine, a less toxic derivative of chloroquine, is effective in inhibiting SARS-CoV-2 infection in vitro, C*ell Discov.*, **6**, 6–9 (2020).
5. P. Gautret, J.-C. Lagier, P. Parola, V. T. Hoang, L. Meddeb, M. Mailhe, B. Doudier, J. Courjon, V. Giordanengo, V. E. Vieira, H. Tissot Dupont, S. Honoré, P. Colson, E. Chabrière, B. La Scola, J.-M. Rolain, P. Brouqui, and D. Raoult, Hydroxychloroquine and azithromycin as a treatment of COVID-19: results of an open-label non-randomized clinical trial, *Int. J. Antimicrob Agents.*, **56(1)**, 105949 (2020).
6. M. L. P. M. Arguelho, J. F. Andrade, and N. R. Stradiotto, Electrochemical study of hydroxychloroquine and its determination in plaquenil by differential pulse voltammetry, *J. Pharm. Biomed. Anal.*, **32(2)**, 269–275 (2003).
7. S. M. Ghoreishi, A. M. Attaran, A. M. Amin, and A. Khoobi, Multiwall carbon nanotube-modified electrode as a nanosensor for electrochemical studies and stripping voltammetric determination of an antimalarial drug, *RSC Adv.,* **5(19)**, 14407–14415 (2015).
8. E. A. Shippey, V. D. Wagler, and A. N. Collamer, Hydroxychloroquine: An old drug with new relevance, *Cleve. Clin. J. Med.*, **85(6)**, 459–467 (2018).
9. W. Wang, L. Liu, Y. Zhou, Q. Ye, X. Yang, J. Jiang, F. Gao, X. Tan, G. Zhang, Q. Fang, and Z. X. Xuan, Hydroxychloroquine enhances the antitumor effects of BC001 in gastric cancer, *Int. J. Onco.*, **55**, 405–414 (2019).
10. F. Keshavarzi, Fungistatic effect of hydroxychloroquine, lessons from a case, *Med. Mycol. Case Rep.*, **13**, 17–18 (2016).
11. M. P. Hage, M. R. Badri, and S. T. Azar, A favorable effect of hydroxychloroquine on glucose and lipid metabolism beyond its anti-inflammatory role, *Ther. Adv. Endocrinol. Metab.*, **5(4)**, 77–85 (2014).
12. T.-Y. Park, Y. Jang, W. Kim, J. Shin, H. T. Toh, C.-H. Kim, H. S. Yoon, P. Leblanc, and K.-S. Kim, Chloroquine modulates inflammatory autoimmune responses through Nurr1 in autoimmune diseases, *Sci. Rep.*, **9**, 15559 (2019).

13. S. Bodur, S. Erarpat, Ö. T. Günkara, and S. Bakırdere, Accurate and sensitive determination of hydroxychloroquinesulfate used on COVID-19 patients in human urine, serum and saliva samples by GC-MS, *J. Pharm. Anal.*, **11(3)**, 278–283 (2021).
14. S. A. Alkahtani, A. M. Mahmoud, M. H. Mahnashi, A. O. AlQarni, Y. S. A. Alqahtani, and M. M. El-Wekil, Facile one pot sonochemical synthesis of layered nanostructure of ZnS NPs/rGO nanosheets for simultaneous analysis of daclatasvir and hydroxychloroquine, *Microchem. J.*, **164**, 105972 (2021).
15. M. A. E. Mhammedi, S. Saqrane, S. Lahrich, F. Laghrib, Y. E. Bouabi, A. Farahi, and M. Bakasse, Current trends in analytical methods for the determination of hydroxychloroquine and its application as treatment for COVID-19, *Chemistry Select*, **5(46)**, 14602–14612 (2020).
16. W.-Y. Chen, Y.-T. Wu, H.-C. Lin, M.-I. Ieong, and B.-H. Lee, Impact of long-term parental exposure to Tamiflu metabolites on the development medaka offspring (Oryzias latipes), *Environ. Pollut.*, **261**, 114146 (2020).
17. B. Tiwari, B. Sellamuthu, Y. Ouarda, P. Drogui, R. D. Tyagi, and G. Buelna, Review on fate and mechanism of removal of pharmaceutical pollutants from wastewater using biological approach, *Bioresour.Technol.*, **224**, 1–12 (2017).
18. S. Dong, L. Cui, Y. Tian, L. Xia, Y. Wu, J. Yu, D. M. Bagley, J. Sun, and M. Fan, A novel and high-performance double Z-scheme photocatalyst ZnO-SnO_2-Zn_2SnO_4 for effective removal of the biological toxicity of antibiotics, *J. Hazard. Mater.*, **399**, 123017 (2020).
19. D. Dabić, S. Babić, and I. Škorić, The role of photodegradation in the environmental fate of hydroxychloroquine, *Chemosphere*, **230**, 268–277 (2019).
20. M. Wang, J. Li, H. Shi, D. Miao, Y. Yang, L. Qian, and S. Gao, Photolysis of atorvastatin in aquatic environment: Influencing factors, products, and pathways, *Chemosphere*, **212**, 467–475 (2018).
21. J. V. Kumar, R. Karthik, S.-M. Chen, V. Muthuraj, and C. Karuppiah, Fabrication of potato-like silver molybdate microstructures for photocatalytic degradation of chronic toxicity ciprofloxacin and highly selective electrochemical detection of H_2O_2, *Sci. Rep.*, **6**, 34149 (2016).
22. K. Phiwdang, S. Suphankij, W. Mekprasart, and W. Pecharapa, Synthesis of CuO nanoparticles by precipitation method using different precursors, *Energy Procedia*, **34**, 740–745 (2013).
23. P. Gao and D. Liu, Hydrothermal preparation of nest-like CuO nanostructures for non-enzymatic amperometric detection of hydrogen peroxide, *RSC Adv.*, **5(31)**, 24625–24634 (2015).
24. W. Z. Teo, A. Ambrosi, and M. Pumera, Direct electrochemistry of copper oxide nanoparticles in alkaline media, *Electrochem. Commun.*, **28**, 51–53 (2013).
25. C. P. Yang, Q. Wu, Z. W. Jiang, X. Wang, C. Z. Huang, and Y. F. Li, Cu vacancies enhanced photoelectrochemical activity of metal-organic gel-derived CuO for the detection of L-cysteine, *Talanta*, **228**, 122261 (2021).
26. Y. Y. Li, P. Kang, S. Q. Wang, Z. G. Liu, Y. X. Li, and Z. Guo, Ag nanoparticles anchored onto porous CuO nanobelts for the ultrasensitive electrochemical detection of dopamine in human serum, *Sens. Actuators B: Chem.*, **327**, 128878 (2021).
27. O. Mahapatra, M. Bhagat, C. Gopalakrishnan, and K. D. Arunachalam, Ultrafine dispersed CuO nanoparticles and their antibacterial activity, *J. Exp. Nanosci.*, **3(3)**, 185–193 (2008).
28. L. Zhang, F. Yuan, X. Zhang, and L. Yang, Facile synthesis of flower like copper oxide and their application to hydrogen peroxide and nitrite sensing, *Chem. Cent. J.*, **5**, 75 (2011).
29. B. Muthukutty, J. Ganesamurthi, S.-M. Chen, B. Arumugam, F. mao chang, S. M. Wabaidur, Z. A. ALOthman, T. Altalhi, and M. A. Ali, Construction of novel binary metal oxides: Copper oxide–tin oxide nanoparticles regulated for selective and nanomolar level electrochemical detection of anti-psychotic drug, *Electrochim. Acta*, **386**, 138482 (2021).
30. S. P. Ashokkumar, H. Vijeth, L. Yesappa, M. Vandana, S. Veeresh, H. Ganesh, Y. S. Nagaraju, and H. Devendrappa, Cyclic voltammetry, morphology and thermal studies of electrochemically synthesized PANI/CuO nanocomposite for supercapacitor application, *AIP Conf. Proc.*, **2244(1)**, 080026 (2020).
31. S.-D. Seo, Y.-H. Jin, S.-H. Lee, H.-W. Shim, and D.-W. Kim, Low-temperature synthesis of CuO-interlaced nanodiscs for lithium ion battery electrodes, *Nanoscale Res. Lett.*, **6**, 397 (2011).
32. L. Dörner, C. Cancellieri, B. Rheingans, M. Walter, R. Kägi, P. Schmutz, M. V. Kovalenko, and L. P. H. Jeurgens, Cost-effective sol-gel synthesis of porous CuO nanoparticle aggregates with tunable specific surface area, *Sci. Rep.*, **9**, 11758 (2019).
33. P. Gao and D. Liu, Petal-like CuO nanostructures prepared by a simple wet chemical method, and their application to non-enzymatic amperometric determination of hydrogen peroxide, *Microchim. Acta*, **182**, 1231–1239 (2015).
34. K. Ganesan, V. K. Jothi, A. Natarajan, A. Rajaram, S. Ravichandran, and S. Ramalingam, Green synthesis of Copper oxide nanoparticles decorated with graphene oxide for anticancer activity and catalytic applications, *Arab. J. Chem.*, **13(8)**, 6802–6814 (2020).
35. S. Sehar, F. Sher, S. Zhang, U. Khalid, J. Sulejmanović, and E. C. Lima, Thermodynamic and kinetic study of synthesised graphene oxide-CuO nanocomposites: A way forward to fuel additive and photocatalytic potentials, *J. Mol. Liq.*, **313**, 113494 (2020).
36. B. Thakur, E. Bernalte, J. P. Smith, C. W. Foster, P. E. Linton, S. N. Sawant, and C. E. Banks, Utilising copper screen-printed electrodes (CuSPE) for the electroanalytical sensing of sulfide, *Analyst*, **141(4)**, 1233–1238 (2016).

37. J. Chen, B. Yao, C. Li, and G. Shi, An improved Hummers method for eco-friendly synthesis of graphene oxide, *Carbon*, **64,** 225–229 (2013).
38. F. Kargar, A. Bemani, M. H. Sayadi, and N. Ahmadpour, Synthesis of modified beta bismuth oxide by titanium oxide and highly efficient solar photocatalytic properties on hydroxychloroquine degradation and pathways, *J. Photochem. Photobiol. A*, **419**, 113453 (2021).
39. T. K. Ghosh, S. Gope, D. Rana, I. Roy, G. Sarkar, S. Sadhukhan, A. Bhattacharya, K. Pramanik, S. Chattopadhyay, M. Chakraborty, and D. Chattopadhyay, Physical and electrical characterization of reduced graphene oxide synthesized adopting green route, *Bull. Mater. Sci.*, **39**, 543–550 (2016).
40. A. S. Sarkar and S. K. Pal, Exponentially distributed trap-controlled space charge limited conduction in graphene oxide films, *J. Phys. D: Appl. Phys.*, **48(44)**, 445501 (2015).
41. D. P. Volanti, D. Keyson, L. S. Cavalcante, A. Z. Simões, M. R. Joya, E. Longo, J. A. Varela, P. S. Pizani, and A. G. Souza, Synthesis and characterization of CuO flower-nanostructure processing by a domestic hydrothermal microwave, *J. Alloys Compd.*, **459(1–2)**, 537–542 (2008).
42. C. Ashok, K. V. Rao, and C. S. Chakra, Structural analysis of CuO nanomaterials prepared by novel microwave assisted method, *J. Atoms Mol.*, **4(5)**, 803–806 (2014).
43. M. I. Din, F. Arshad, A. Rani, A. Aihetasham, M. Mukhtar, and H. A. mehmood, Single step green synthesis of stable copper oxide nanoparticles as efficient photo catalyst material, *J. Optoelectron. Biomed. Mater.*, **9(1)**, 41–48 (2017).
44. P. K. Raul, S. Senapati, A. K. Sahoo, I. M. Umlong, R. R. Devi, A. J. Thakur, and V. Veer, CuO nanorods: A potential and efficient adsorbent in water purification, *RSC Adv.*, **4**, 40580–40587 (2014).
45. M. S. Treasa and J. Premakumari, Characterisation and solubility studies of Quinine sulphate and Hydroxychloroquine sulphate inclusion complexes with α – cyclodextrin, *IOSR J. Appl. Chem.*, **11(11)**, 24–34 (2018).
46. P. P. Brisebois, R. Izquierdo, and M. Siaj, Room-temperature reduction of graphene oxide in water by metal chloride hydrates: A cleaner approach for the preparation of graphene@metal hybrids, *Nanomaterials.*, **10(7)**, 1255. (2020)
47. R. Hidayat, S. Wahyuningsih, and A. H. Ramelan, Simple synthesis of rGO (reduced graphene oxide) by thermal reduction of GO (graphene oxide), *IOP Conf. Ser.: Mater. Sci. Eng.*, **858**, 012009 (2020).
48. A. N. F. Moraes, L. A. D. Silva, M. A. de Oliveira, E. M. de Oliveira, T. L. Nascimento, E. M. Lima, I. M. S. Torres, and D. G. A. Diniz, Compatibility study of hydroxychloroquine sulfate with pharmaceutical excipients using thermal and nonthermal techniques for the development of hard capsules, *J. Therm. Anal. Calorim.*, **140**, 2283–2292 (2020).
49. S.-L. Cheng and M.-F. Chen, Fabrication, characterization, and kinetic study of vertical single-crystalline CuO nanowires on Si substrates, *Nanoscale Res. Lett.*, **7**, 119 (2012).
50. S.-L. Cheng, M. F. Chen, and C. H. Chung, Synthesis and growth kinetics of large-scale CuO nanowires grown by oxidation of Cu films, *The 4th IEEE International NanoElectronics Conference*, Taoyuan, Taiwan, pp. 1–2 (2011).
51. X. Zhu, H. Shi, J. Yin, H. Zhu, Y. Zhou, Y. Tang, P. Wu, and T. Lu, Facile preparation of CuO@SnO_2 nanobelts as a high-capacity and long-life anode for lithium-ion batteries, *RSC Adv.*, **4**, 34417–34420 (2014).
52. P. L. da Silva, R. P. Nippes, P. D. Macruz, F. L. Hegeto, and M. H. N. O. Scaliante, Photocatalytic degradation of hydroxychloroquine using ZnO supported on clinoptilolite zeolite, *Water Sci. Technol.*, **84(3)**, 763–776 (2021).
53. J. de Oliveira S. Silva, M. V. S. SantAnna, A. Gevaerd, J. B. S. Lima, M. D. S. Monteiro, S. W. M. M. Carvalho, and E. M. Sussuchi, A novel carbon nitride nanosheets-based electrochemical sensor for determination of hydroxychloroquine in pharmaceutical formulation and synthetic urine samples, *Eelectroanalysis*, **33(10)**, 2152–2160. (2021)
54. J. Ghasemi, A. Niazi, and R. Ghorbani, Determination of trace amounts of lorazepam by adsorptive cathodic differential pulse stripping method in pharmaceutical formulations and biological fluids, *Analytical Letters*, **39(6)**, 1159–1169 (2006).
55. P. A. Pushpanjali, J. G. Manjunatha, N. Hareesah, T. Girish, A. A. Al-Kahtnai, M. Tighezza, and N. Ataollahi, Electrocatalytic determination of hydroxychloroquine using sodium dodecyl sulphate modified carbon nanotube paste electrode, *Top. Catal.*, (2022). https://doi.org/10.1007/s11244-022-01568-8
56. J. Ning, Q. He, X. Luo, M. Wang, D. Liu, J. Wang, J. Liu, and G. Li, Rapid and sensitive determination of vanillin based on a glassy carbon electrode modified with Cu_2O-electrochemically reduced graphene oxide nanocomposite film, *Sensors*, **18(9)**, 2762 (2018).
57. Y. Zheng, A. Wang, H. Lin, L. Fu, and W. Cai, A sensitive electrochemical sensor for direct phoxim detection based on an electrodeposited reduced graphene oxide-gold nanocomposite, *RSC Adv.*, **5(20)**, 15425–15430 (2015).
58. H. Zhang, L. Cheng, H. Shang, W. Zhang, and A. Zhang, A novel electrochemical sensor based on reduced graphene oxide–TiO_2 nanocomposites with high selectivity for the determination of hydroxychloroquine, *Russ. J. Electrochem.*, **57**, 872–884 (2021).
59. H. M. Mahnashi, A. M. Mahmoud, A. S. Alkahtani, and M. M. El-Wekil, Simultaneous electrochemical detection of azithromycin and hydroxychloroquine based on VS_2 QDs embedded N, S @graphene aerogel/cCNTs 3D nanostructure, *Microchem. J.*, **163**, 105925 (2021).
60. D. M. de Ara, S. M. Paiva, J. M. M. Henrique, C. A. Martínez-Huitle, and E. V. D. Santos, Green composite

sensor for monitoring hydroxychloroquine in different water matrix, *Materials*, **14(17)**, 4990 (2021).
61. P. Balasubramanian, T. S. T. Balamurugan, C. Shen-Ming, C. Tse-Wei, G. Sharmila, and Y. Ming-Chin, One-step green synthesis of colloidal gold nano particles?: A potential electrocatalyst towards high sensitive electrochemical detection of methyl parathion in food samples, *J. Taiwan Inst. Chem. Eng.*, **87**, 83–90 (2018).
62. F. Peng, Y. Sun, Y. Lu, W. Yu, M. Ge, J. Shi, R. Cong, J. Hao, and N. Dai, Studies on sensing properties and mechanism of CuO nanoparticles to H_2S Gas, *Nanomaterials*, **10(4)**, 774 (2020).
63. S. Reddy, B. E. K. Swamy, and H. Jayadevappa, CuO nanoparticle sensor for the electrochemical determination of dopamine, *Electrochim. Acta*, **61**, 78–86 (2012).
64. B. Avinash, C. R. Ravikumar, M. R. A. Kumar, H. P. Nagaswarupa, M. S. Santosh, A. S. Bhatt, and D. Kuznetsov, Nano CuO: Electrochemical sensor for the determination of paracetamol and d-glucose, *J. Phys. Chem. Solids*, **134**, 193–200 (2019).
65. J. Zoubir, I. Bakas, S. Qourzal, M. Tamimi, and A. Assabbane, Electrochemical sensor based on a ZnO-doped graphitized carbon for the electrocatalytic detection of the antibiotic hydroxychloroquine. Application: tap water and human urine, *J. Appl. Electrochem.*, **53**, 1279–1294 (2023).
66. M. S. Carvalho, R. G. Rocha, L. V. de Faria, E. M. Richter, L. M. F. Dantas, I. S. da Silva, and R. A. A. Muñoz, Additively manufactured electrodes for the electrochemical detection of hydroxychloroquine, *Talanta*, **250**, 123727 (2020).
67. W. Wang, J. C. Yu, D. Xia, P. K. Wong, and Y. Li, Graphene and g-C_3N_4 nanosheets cowrapped elemental α-sulfur as a novel metal-free heterojunction photocatalyst for bacterial inactivation under visible-light, *Environ. Sci., Technol.*, **47(15)**, 8724–8732 (2013).
68. J. Yu, J. Jin, B. Cheng, and M. Jaroniec, A noble metal-free reduced graphene oxide-cds nanorod composite for the enhanced visible-light photocatalytic reduction of CO_2 to solar fuel, *J. Mater. Chem. A*, **2(10)**, 3407–3416 (2014).
69. M. Kaur, A. Umar, S. K. Mehta, and S. K. Kansal, Reduced graphene oxide-CdS heterostructure: An efficient fluorescent probe for the sensing of Ag(I) and sunset yellow and a visible-light responsive photocatalyst for the degradation of levofloxacin drug in aqueous phase, *Appl. Catal. B*, **245**, 143–158 (2019).
70. T. S. Anirudhan and J. R. Deepa, Nano-zinc oxide incorporated graphene oxide/nanocellulose composite for the adsorption and photo catalytic degradation of ciprofloxacin hydrochloride from aqueous solutions, *J. Colloid Interface Sci.*, **490**, 343–356 (2017).
71. B. Saini and G. Bansal, Characterization of four new photodegradation products of hydroxychloroquine through LC-PDA, ESI-MS^n and LC-MS-TOF studies, *J. Pharm. Biomed. Anal.*, **84**, 224–231 (2013).
72. M. C. Rath, S. J. Keny, H. P. Upadhyaya, S. Adhikari, Free radical induced degradation and computational studies of hydroxychloroquine in aqueous solution, *Radiat. Phys. Chem.*, **206**, 110785 (2023).